Lab on a Chip

PAPER

View Article Online
View Journal | View Issue

Cite this: *Lab Chip*, 2025, **25**, 5914

Electrical impedance tomography (EIT)-based intracellular conductivity imaging for non-invasive cell detection

Songshi Li, [a] Daisuke Kawashima, *[ab] Zeyang Dai,[a] Nobuyuki Aoki[c] and Masahiro Takei[ab]

Electrical impedance tomography (EIT)-based intracellular conductivity imaging is newly proposed as a non-invasive technique for mapping the electrical properties of living cells at the single-cell scale. In order to achieve this, a micro-EIT system is developed, which integrates two main components: a custom-designed micro-EIT sensor and a frequency-differential EIT coupled with a single-cell equivalent circuit-based reconstruction algorithm. The micro-EIT sensor is designed to match single-cell scale and fabricated on a glass substrate by electron beam lithography, which enables high spatial resolution (7 μm electrode width, 40 μm spacing), stable frequency response, and signal-to-noise ratios typically ranging from 50 to 200. The frequency-difference EIT achieves the reconstruction of conductivity distributions of the cytoplasm σ_{cyt} and nucleoplasm σ_{nuc} through current response analysis based on the equivalent circuit model of a single cell. To evaluate the performance, impedance spectra were measured to reconstruct the intracellular conductivity images in three types of Medical Research Council 5 (MRC-5) human lung fibroblast cell lines with different protein expressions. As a result, σ_{cyt} and σ_{nuc} of three cell types were successfully reconstructed, which revealed clear differences corresponding to variations in protein expression. Brightfield and fluorescence observations were also performed to verify the EIT results, which demonstrated the reliability of the coordinates and the size of the cytoplasm and nucleoplasm. This work represents the first demonstration of non-invasive intracellular conductivity mapping that distinguishes subcellular structures based on electrical properties.

Received 12th May 2025,
Accepted 29th September 2025

DOI: 10.1039/d5lc00466g

rsc.li/loc

1 Introduction

Understanding and visualizing the electrical properties of individual living cells, particularly intracellular conductivity, has become increasingly important in biomedical research, with applications in cancer cell analysis,[1] stem cell engineering,[2] and drug development.[3] Traditionally, such measurements relied on invasive techniques like microelectrode insertion,[4] microinjection,[5] and cell lysis,[6] which disturb cellular integrity and hinder real-time analysis. As a non-invasive and label-free alternative, single-cell conductivity measurement offers a powerful tool for analysing the dynamic electrical responses of living cells in their natural state.

To meet this demand, the combination of microelectrode technique and electrical impedance spectroscopy (EIS) is applied to measure single-cell conductivity.[7,8] An EIS-based biosensor coupled with a microfluidic platform was designed and fabricated to investigate the formation process of the primary cell wall (PCW) at the single-cell level, which indicated that PCW formation caused a dramatic change in cell electrical conductivity.[9] EIS with impedance measurements at various voltages and frequencies was presented to differentiate four kinds of cells (HeLa, A549, MCF-7, and MDA-MB-231) by measuring the single-cell electrical properties.[10] Nevertheless, the EIS-based single-cell measurement does not meet the needs of spatial information in single-cell analysis.[11]

Electrical impedance tomography (EIT) offers a spatial information approach to single-cell measurement by reconstructing conductivity distribution.[12–14] An EIT-based impedance–optical dual-modal imaging was developed for high-quality monitoring of cell spheroid cultures by efficiently fusing images from EIT and microscopy to generate final conductivity images.[15] Another EIT method incorporated a second-order sensitivity matrix that detected the heterogeneity of cell spheroids by imaging the conductivity with a 1 mm microsensor.[16] Nonetheless, these

[a] *Graduate School of Engineering, Chiba University, 1-33 Yayoi, Inage, Chiba, 263-8522 Japan. E-mail: dkawa@chiba-u.jp*
[b] *Center of Quantum Life Science for Structural Therapeutics (cQUEST), Chiba University, 1-33 Yayoi, Inage, Chiba, 263-8522 Japan*
[c] *Department of Materials Science, Chiba University, 1-33 Yayoi, Inage, Chiba, 263-8522 Japan*

studies primarily focus on multicellular systems, such as spheroid cultures, where the resolution and sensitivity of EIT are sufficient for their scale. Despite its advantages, EIT faces significant challenges in achieving single-cell imaging primarily due to insufficient spatial resolution, which affects the ability to distinguish fine intracellular structures and reconstruct conductivity distributions at the single-cell scale.

Single-cell imaging was proposed by developing a rolled-up microtubular sensor with a diameter of 30 μm to study the electrical properties of individual cells for monitoring the death of a single HeLa cell over time.[17] However, the EIT images did not reflect a reasonable intracellular conductivity distribution of a single cell due to (1) the large electrode size in the direction perpendicular to the imaging plane, which caused a lack of spatial resolution, and (2) the frequency selection in the frequency-difference EIT (fdEIT), which was not sufficiently tailored to the electrical properties of single cells.

To achieve intracellular conductivity imaging, our approach is (1) to develop a micro-EIT sensor with a smaller size in the direction perpendicular to the imaging plane, to satisfy the spatial resolution requirement of intracellular conductivity distribution, and (2) to optimize the frequency selection in fdEIT based on an equivalent circuit model of a

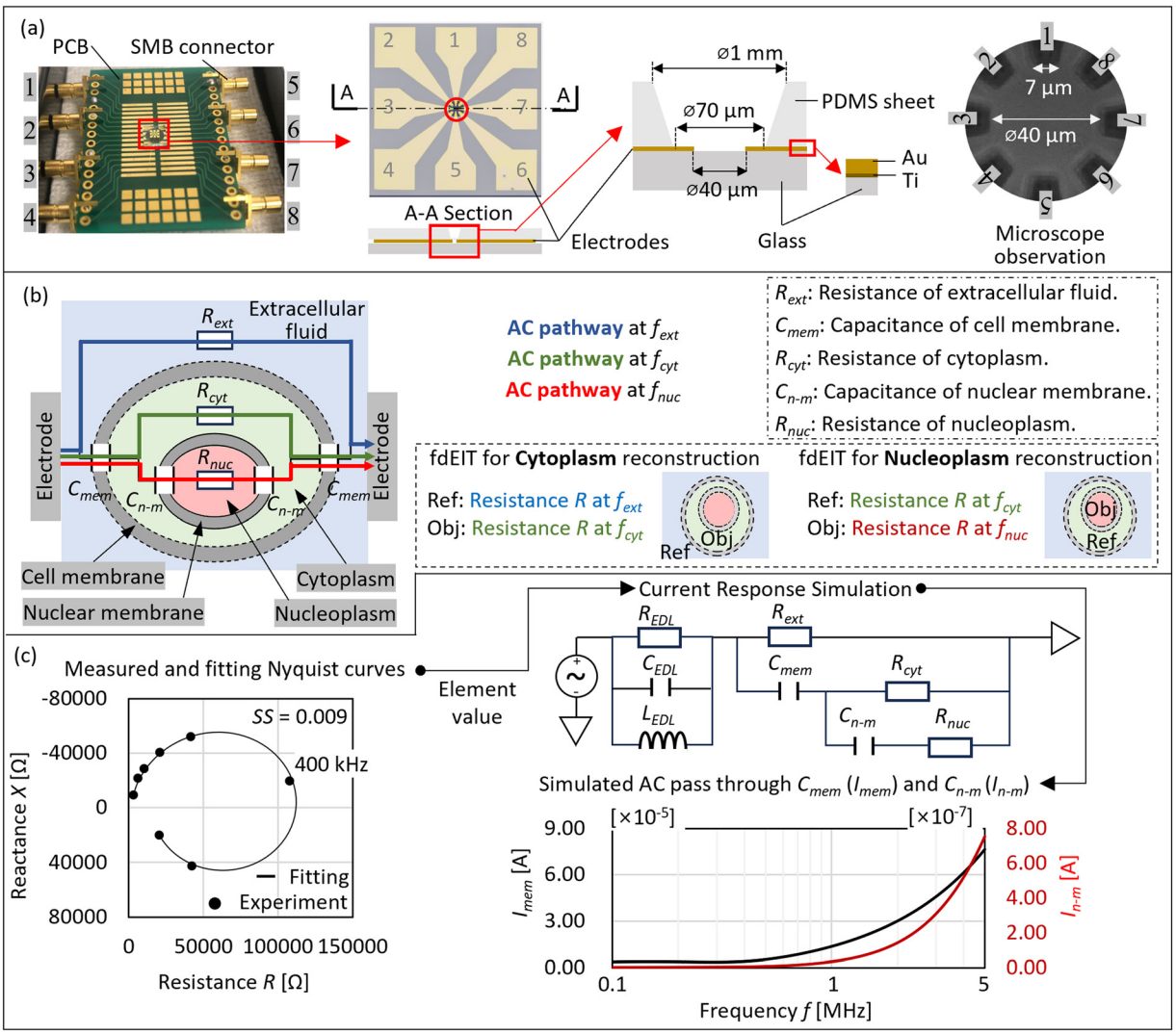

Fig. 1 Materials and methods for intracellular conductivity imaging. (a) Schematic of the custom-designed micro-EIT sensor fabricated by electron beam lithography and metal deposition. Gold (Au, 50 nm) and titanium (Ti, 5 nm) layers are deposited on a glass substrate to form eight electrodes (7 μm width, 40 μm spacing), arranged azimuthally at 45° intervals to enable single-cell-scale impedance measurement. (b) Concept of frequency-difference EIT (fdEIT) and the equivalent AC current pathways at three selected frequencies: fdEIT based on the AC pathway at f_{ext} (extracellular dominant), f_{cyt} (cytoplasmic dominant) and f_{nuc} (nucleoplasm dominant). These frequencies are selected to selectively probe different subcellular compartments based on their dielectric properties. (c) Experimental and simulated data for system validation. Left: Nyquist curves of measured impedance spectra and the corresponding fitting using the single-cell equivalent circuit model. Upper right: current response simulation circuit constructed in SPICE, illustrating key electrical elements and their interconnections. Lower right: simulated AC components passing through the cell membrane capacitance C_{mem} and nuclear membrane capacitance C_{n-m}, which demonstrates frequency-dependent intracellular current distribution.

single cell, to tailor more effectively to the electrical properties of single cells for more precise reconstruction of intracellular conductivity distribution.

The objectives of this study are (1) to propose electrical impedance tomography (EIT)-based intracellular conductivity imaging while developing a micro-EIT sensor and analysing frequency response by equivalent circuit and current response simulation, (2) to apply EIT-based intracellular conductivity imaging to reconstruct the intracellular conductivity distribution of three types of cells with different protein expression and (3) to verify the EIT results by microscopic observation and equivalent circuit analysis.

2 Materials and methods

2.1 Micro-EIT sensor

A newly developed micro-EIT sensor for intracellular conductivity imaging is introduced. Fig. 1(a) shows the schematic of the newly developed micro-EIT sensor based on electron beam lithography and deposition for reconstructing the intracellular conductivity distribution of a single cell. The electrodes of the micro-EIT sensor are deposited on a glass substrate by electron beam lithography and electron beam deposition of titanium (Ti) and gold (Au).[18] The Ti layer (thickness of 5 nm) is positioned between the glass substrate and the Au layer, which serves as an adhesion layer to bond the glass substrate with the Au layer. The Au layer (thickness of 50 nm) is in direct contact with the sample for impedance measurement. The micro-EIT sensor has 8 electrodes which are 7 μm wide, separated by 40 μm and aligned with an azimuthal angle of 45°. A polydimethylsiloxane (PDMS) sheet with a corn-shaped hole structure is placed aligned in the center of the micro-EIT sensor on the glass substrate and electrodes. The top and the bottom sizes of the hole are 1 mm and 70 μm, respectively, to control the single cell within the sensor area. The glass substrate is settled on a plastic circuit board (PCB), which has an inspection hole at the center to allow the micro-EIT sensor to be observed with an optical microscope. After wiring between the electrodes and the pads on the PCB with gold-ball bonding, all the electrodes including bonding wires are covered and hardened with epoxy to protect them. The PCB is soldered with 8 subminiature version B (SMB) connectors, which are connected to a multiplexer.

2.2 Frequency-difference electrical impedance tomography (fdEIT) with spectral analysis

Fig. 1(b) shows the fdEIT with spectral analysis to reconstruct the intracellular conductivity distribution. An equivalent circuit of a single cell, which includes resistance of extracellular fluid R_{ext}, capacitance of cell membrane C_{mem}, resistance of cytoplasm R_{cyt}, capacitance of nuclear membrane $C_{n\text{-}m}$ and resistance of nucleoplasm R_{nuc}, is applied to analyse the alternating current (AC) pathway at different frequencies. Based on the capacitive property of the cell membrane and the nuclear membrane,[19] the AC sequentially passes through the extracellular fluid (AC pathway at f_{ext} in blue), cytoplasm (AC pathway at f_{cyt} in green) and nucleoplasm (AC pathway at f_{nuc} in red) as the frequency f [Hz] increases. For the reconstruction of cytoplasm conductivity distribution, R at f_{ext}, where the AC (blue) passes only through the extracellular fluid, serves as the reference data, and R at f_{cyt}, where the AC (green) passes through the extracellular fluid and cytoplasm, serves as the objective data. The conductivity distribution of the cytoplasm can be reconstructed based on the difference in conductivity between the extracellular fluid and the cytoplasm.[20] For the reconstruction of nucleoplasm conductivity distribution, R at f_{cyt}, where the AC (green) passes through the extracellular fluid and cytoplasm, serves as the reference data, and f_{nuc}, where the AC (red) passes through the extracellular fluid, cytoplasm and nucleoplasm, serves as the objective data. The conductivity distribution of the nucleoplasm can be reconstructed based on the difference in conductivity between the cytoplasm and the nucleoplasm.[20]

In order to determine f_{ext}, f_{cyt} and f_{nuc}, equivalent circuit analysis and AC simulation are performed. Fig. 1(c), left, shows the measured and fitting Nyquist curves. The experimental data present the Nyquist curve of single-cell measurements within the frequency range of 100 kHz to 5 MHz, with experimental details provided in section 3 (Experiments). The measured resistance R at the frequency f_{ext} = 400 kHz, where R reaches its maximum (the rightmost point of the Nyquist curve), represents the extracellular fluid.[21] By fitting the equivalent circuit which is provided in section 4.4 (Electrical properties of single cells), the element values in the equivalent circuit are obtained, and the fitting curve shown in Fig. 1(c), left, demonstrates a good level of agreement with a sum of squares SS = 0.009. Based on the fitted element values by the equivalent circuit, current response simulation was performed to investigate the current response of C_{mem} and $C_{n\text{-}m}$. Fig. 1(c), upper right, shows the current response simulation by LTspice, which is a SPICE simulator software program.[22] The equivalent circuit and element value are the same as provided in section 4.4. Fig. 1(c), lower right, shows the simulated current passing through C_{mem} and $C_{n\text{-}m}$. At frequencies below 400 kHz, the AC through C_{mem} (I_{mem}) and $C_{n\text{-}m}$ ($I_{n\text{-}m}$) shows no significant change due to the inability of the AC to pass through C_{mem} at this frequency, which confirms that f_{ext} = 400 kHz. As f increases, I_{mem} and $I_{n\text{-}m}$ gradually increase. At f = 1 MHz, I_{mem} is increased significantly, while $I_{n\text{-}m}$ shows a slight increase, which indicates that cytoplasm information is dominant at this frequency. Therefore, 1 MHz is determined as f_{cyt}.[16] At 5 MHz, $I_{n\text{-}m}$ reaches the maximum value, which indicates the strongest nucleoplasm signal. Therefore, 5 MHz is determined as f_{nuc}.

3 Experiments

3.1 Cell culture and sample preparation

Three types of Medical Research Council 5 (MRC-5) human lung fibroblast cell line are measured in this study: wild type (WT), histone-GFP type (HT) and GFP type (GFPT).[23] WT is the common type of MRC-5, HT is the MRC-5 with the transfection of green fluorescent protein (GFP)-fused histone in the nucleoplasm and GFPT is the MRC-5 with the transfection of GFP in the cytoplasm.[24] MRC-5 cells were plated in low glucose medium which is composed of 89% Dulbecco's modified Eagle medium (DMEM, Gibco, USA), 10% fetal bovine serum (FBS, 35-079-CV, Corning, USA) and 1% penicillin/streptomycin (P/S, Gibco, USA). MRC-5 cells were cultured in an incubator (MCO-18AIC (UV), Sanyo, Japan) at 37 °C and 5% CO_2 in air. MRC-5 cells were passaged every three days with 6 cm culture dishes (3353002, Falcon, USA). In the EIT experiments, a cell–phosphate-buffered saline (PBS) suspension was made and placed on the micro-EIT sensor.

3.2 Experimental setup

Fig. 2 shows the micro-EIT imaging system, which includes a micro-EIT sensor for EIT measurement, a multiplexer for electrode switching, an impedance analyzer (IM3570, Hioki, Japan) for impedance measurement, a pneumatic microinjector (IM-11-2, Narishige, Japan) for cell controlling, a microscope (Eclipse Ti2-E, Nikon, Japan) with a 40× objective lens (Plan Fluor ELWD 40× DIC M N1, Nikon, Japan) for observing cells and a PC for system controlling.

3.3 Experimental conditions and methods

Adherent cultured MRC-5 cells were added to a 3.5 cm dish after being made into a low concentration cell–PBS–sucrose suspension. Under microscopic observation, one cell and 2 μL medium were extracted from the dish by pneumatic microinjector and then placed on the micro-EIT sensor through the hole of the PDMS sheet. After that, microscopy observations and EIT measurements were started simultaneously. The 2-terminal model method, where the current excitation (Lc, Hc) and voltage measurement (Lp, Hp) are conducted on the same electrode pair,[25] was applied in EIT measurements with the electrode combination number M = 28. The 2-terminal model method was selected because unlike the 4-terminal model method which measures transfer impedance,[26] the 2-terminal model provides direct impedance measurements that are more suitable for impedance spectral analysis. The current excitation electrode pair is connected to the Lc and Hc terminals, and the voltage measurement pair is connected to the Lp and Hp terminals. The excitation current I is 0.01 mA, and the frequencies are 0.1, 0.2, 0.4, 0.7, 1, 1.5, 2 and 5 MHz. Prior to cell measurements, a PBS–sucrose solution was measured to validate the performance of the micro-EIT sensor. The PBS–sucrose solution was prepared by mixing PBS and a 50 mM sucrose aqueous solution at a volume ratio of 1 : 15, with the 50 mM sucrose concentration selected based on our previous research.[27] The excitation current and frequencies were the same as the cell measurements.

3.4 EIT reconstruction

In EIT measurement, complex impedance $\mathbf{Z}^*$ [Ω], phase angle $\boldsymbol{\theta}$ [°], resistance $\mathbf{R}$ [Ω] and reactance $\mathbf{X}$ [Ω] are obtained as follows:

$$\mathbf{Z}^* = [\mathbf{Z}^{*1}, \mathbf{Z}^{*2}, \cdots, \mathbf{Z}^{*l}, \cdots, \mathbf{Z}^{*L}] \in \mathbb{C}^{M \times L} \quad (1a)$$

$$\boldsymbol{\theta} = [\boldsymbol{\theta}^1, \boldsymbol{\theta}^2, \cdots, \boldsymbol{\theta}^l, \cdots, \boldsymbol{\theta}^L] \in \mathbb{R}^{M \times L} \quad (1b)$$

$$\mathbf{R} = [\mathbf{R}^1, \mathbf{R}^2, \cdots, \mathbf{R}^l, \cdots, \mathbf{R}^L] \in \mathbb{R}^{M \times L} \quad (1c)$$

$$\mathbf{X} = [\mathbf{X}^1, \mathbf{X}^2, \cdots, \mathbf{X}^l, \cdots, \mathbf{X}^L] \in \mathbb{R}^{M \times L} \quad (1d)$$

where m ($1 \le m \le M$) is the index of electrode combination, and l ($1 \le l \le L$) is the index of measurement frequency. $\mathbf{R}$ and $\mathbf{X}$, which serve to create the Nyquist plots for electrical impedance spectroscopy (EIS) analysis, are the real and imaginary parts of $\mathbf{Z}^*$.[28]

In the image reconstruction, the forward problem for Jacobian calculation and the inverse problem for conductivity reconstruction need to be solved.[29] In the forward problem, the Jacobian matrix $\mathbf{J}$ is calculated by simulation with a homogeneous conductivity distribution σ_n = 1 in EIDORS software (ver. 3.10)[30] as follows:

$$J_{m,n} = \frac{\partial v_m}{\partial \sigma_n} = \int_\Omega \nabla u(i^e) \cdot \nabla u(i^m) \mathrm{d}\Omega \quad (2)$$

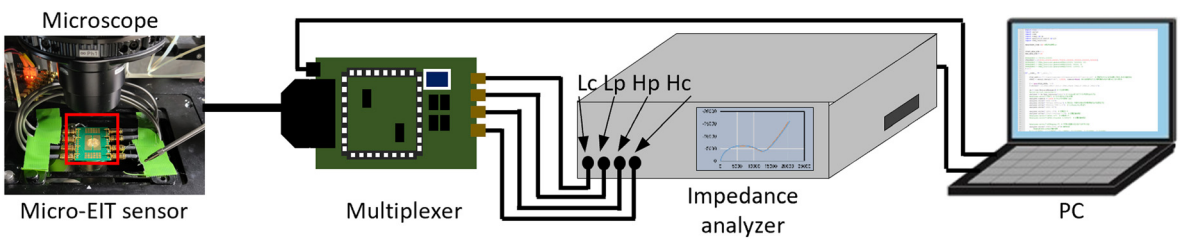

Fig. 2 Micro-EIT imaging system, which includes a micro-EIT sensor, a multiplexer, an impedance analyzer, a pneumatic microinjector, a microscope, and a PC.

where n ($1 \le n \le N$) is the mesh number, $J_{m,n}$ is the Jacobian matrix element of the mth measured pattern in the nth mesh, v_m is the measurement voltage at the mth electrode combination and σ_n is the conductivity at the nth mesh. $u(i^e)$ is

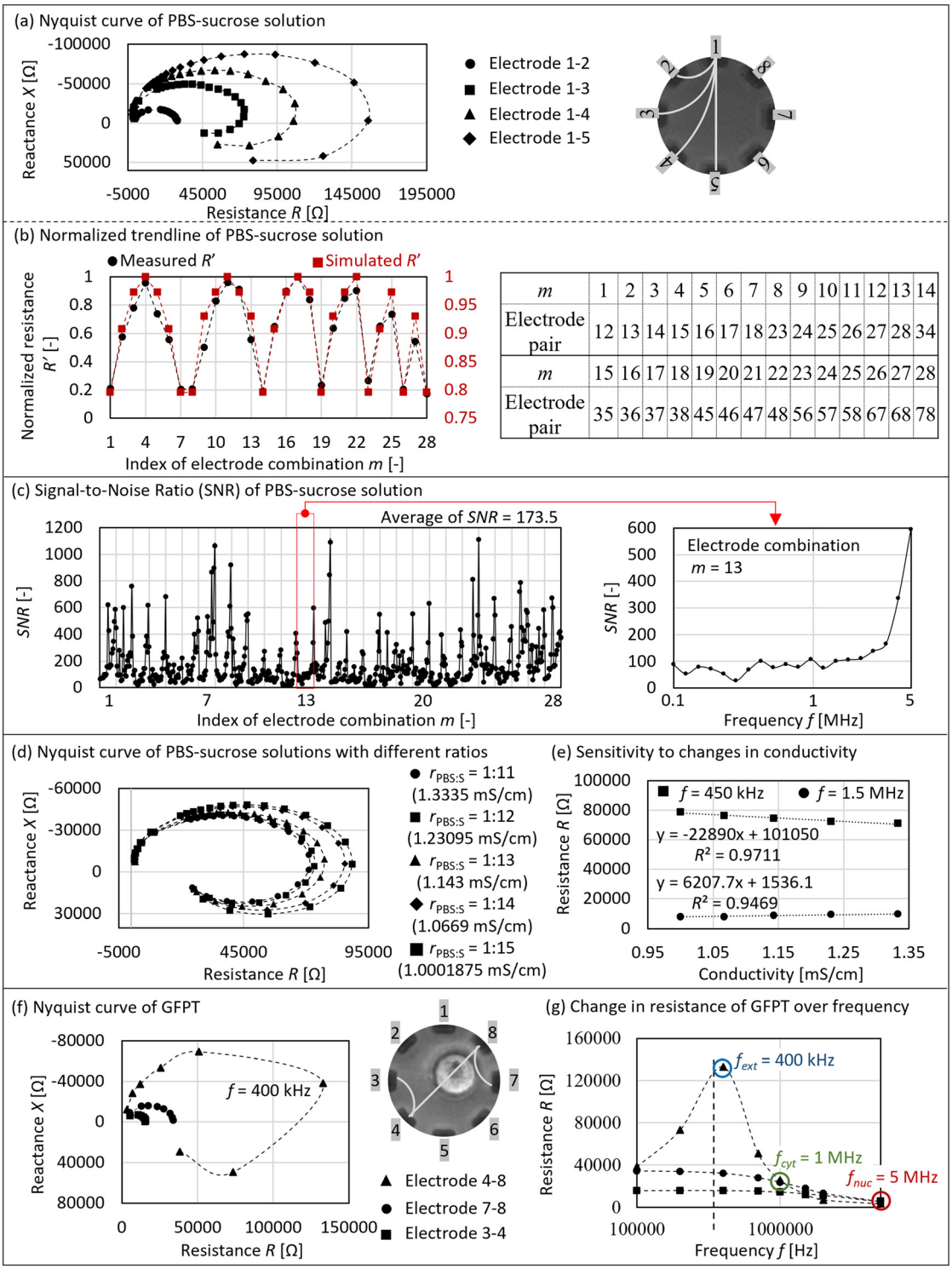

Fig. 3 Measurement results. (a) Nyquist curves of PBS–sucrose solution at different electrode pairs 1-2, 1-3, 1-4 and 1-5. (b) Normalized trend lines of PBS–sucrose solution measurement and simulation, demonstrating the system's spatial resolution capability. (c) SNR mapped across all electrode combinations and frequencies, providing a quantitative evaluation of the measurement stability and overall sensor performance. (d) Impedance responses of PBS–sucrose solutions with varying ratios of PBS and sucrose. (e) Sensitivity to changes in conductivity at f = 450 kHz and 1.5 MHz. (f) Nyquist curves of GFPT measured at electrode pairs 4-8, 7-8 and 3-4. (g) R–f plots of GFPT measured at electrode pairs 4-8, 7-8 and 3-4.

the potential field generated by injecting current i into the eth electrode, $u(i^m)$ is the potential field generated by injecting current i into the mth measured voltage pattern and Ω is the electrical field area of the micro-EIT sensor. In the inverse problem, conductivity $\boldsymbol{\sigma}$ is reconstructed from $\mathbf{R}$ as follows:

$$\boldsymbol{\sigma} = \mathbf{J}^T\Delta\mathbf{R} - \left(\mathbf{J}^T\mathbf{J} + \mu\mathbf{I}\right)^{-1}\mathbf{J}^T\Delta\mathbf{R} \tag{3}$$

where μ is the hyperparameter, $\mathbf{I}$ is the regularization matrix of Tikhonov prior,[31] and $\Delta\mathbf{R}$ is the frequency-normalized resistance difference between the measured resistance of a cell at two frequencies.[32] The Gauss–Newton iterative method was applied to calculate $\boldsymbol{\sigma}$.[33] $\Delta\mathbf{R}$ is described as follows:

$$\Delta\mathbf{R} = \frac{\mathbf{R}_{f2} - a\mathbf{R}_{f1}}{\max\left(\mathbf{R}_{f1}\right)} \quad a = \frac{\left\langle \mathbf{R}_{f1},\ \mathbf{R}_{f2}\right\rangle}{\left\langle \mathbf{R}_{f1},\ \mathbf{R}_{f1}\right\rangle} \tag{4}$$

where $\mathbf{R}_{f1}$ and $\mathbf{R}_{f2}$ are the measurement resistance of the cell at f1th (reference frequency) and f2th (objective frequency) frequencies, a is a frequency weight factor and $\langle\bullet,\bullet\rangle$ is the standard inner product of two vectors.

4 Results and discussion

4.1 Measurement results

Fig. 3 shows the measurement results. Fig. 3(a) shows the Nyquist curves of PBS–sucrose solution measured at electrode pairs 1-2, 1-3, 1-4 and 1-5. The diameters of the Nyquist curves from electrode pairs 1-2 to 1-5 gradually increased due to the impedance increasing with the measurement distance. The arc shape and diameter changes of the Nyquist curve demonstrate the strong performance of the developed micro-EIT sensor. Fig. 3(b) shows the normalized trend lines of PBS–sucrose solution measurement and simulation, where m ($1 \le m \le 28$) is the index of electrode combination and R' is the normalized resistance which is calculated by $\mathbf{R}' = \mathbf{R}/\max(\mathbf{R})$. The simulated R' (red squares) was calculated in the forward problem under the same conditions as the simulation of $\mathbf{J}$. The measured R' (black dots) fully reflected the relationship between electrode distances and R. The measured and simulated R' exhibit very similar trend lines, which also demonstrate an excellent performance of the micro-EIT sensor. Fig. 3(c) shows the signal-to-noise ratio (SNR) of each electrode combination and frequency to further assess the performance of the micro-EIT sensor. The SNR was calculated based on 30 repeated measurements of the PBS–sucrose solution as follows:

$$\mathrm{SNR}_{i,j} = \frac{\left|R_{i,j}\right|}{s_{i,j}} \tag{5}$$

$$\bar{R}_{i,j} = \frac{1}{N}\sum_{k=1}^{N} R_{i,j}^{(k)} \tag{6}$$

$$s_{i,j} = \sqrt{\frac{1}{N}\sum_{k=1}^{N}\left(R_{i,j}^{(k)} - \bar{R}_{i,j}\right)^2} \tag{7}$$

where $\bar{R}_{i,j}$ is the average resistance at electrode pair i and frequency index j, $s_{i,j}$ is the standard deviation, and $N = 30$ is the number of repeated measurements. The SNR plot for all electrode pairs shows that except for a few high-frequency cases where the SNR exceeds 200, the majority of SNRs lie between 50 and 100, with an overall average SNR of 173.5. The SNR of electrode pair $m = 13$ shows a stable range between 50 and 100 below 2 MHz, then sharply rises to approximately 600 above 2 MHz. Fig. 3(d) shows the measurement results of PBS–sucrose solutions with different volume ratios of PBS to sucrose solution ($r_{\mathrm{PBS:S}}$ = 1 : 11, 1 : 12, 1 : 13, 1 : 14 and 1 : 15) to investigate the sensitivity of the micro-EIT sensor. The Nyquist plots demonstrate that as the proportion of sucrose increases, the arc radius gradually becomes larger, which indicates a decrease in conductivity. This is because the conductivity of sucrose solution is significantly lower than that of PBS. Fig. 3(e) shows the sensitivity to changes in conductivity. The conductivity of the PBS–sucrose solutions with $r_{\mathrm{PBS:S}}$ = 1 : 11, 1 : 12, 1 : 13, 1 : 14 and 1 : 15 was calculated based on the known conductivities of PBS (16 mS cm^{-1})[34] and sucrose solution (0.0002 mS cm^{-1}) using a volume-weighted averaging method. This approach assumes that no chemical reactions or significant changes in ion concentration occur upon mixing, which holds true for PBS and sucrose solutions.[35] The calculated conductivity of PBS–sucrose solutions with $r_{\mathrm{PBS:S}}$ = 1 : 11, 1 : 12, 1 : 13, 1 : 14 and 1 : 15 was 1.334, 1.231, 1.143, 1.067, and 1.000 mS cm^{-1}, respectively. The measured R at f = 450 kHz and 1.5 MHz was plotted against the calculated conductivity, and trend lines with coefficients of determination (R^2) were obtained. The results demonstrate good sensitivity of the measurement to changes in conductivity. Fig. 3(f) shows the Nyquist curves of GFPT at electrode pairs 7-8 (close to cell), 3-4 (far from cell) and 4-8 (cross cell) as examples. The diameters of the Nyquist curves measured at electrode pairs 7-8 and 3-4 were similar due to the same electrode distances, with the difference arising from the influence of the cell. The diameter measured at electrode pair 4-8 was large due to the large electrode distance along with the inclusion of cell information. This trend was also observed in the results of WT and HT, which was considered to be due to the higher conductivity of the cell.[36] Fig. 3(g) shows the change in R of GFPT over f. The R measured at electrode pairs 7-8 and 3-4 exhibited a minor change over f. The R measured at electrode pair 4-8 exhibited an initial increase followed by a decrease over f. Based on the frequency analysis of impedance from electrode pair 4-8 shown in section 2.2 (Frequency-difference electrical impedance tomography (fdEIT) with spectral analysis), R at the frequency f_{ext} = 400 kHz, where R reaches its maximum (the rightmost point of the Nyquist curve shown in Fig. 3(c)), represents the extracellular fluid.[21] As the frequency increases, the current fully passes through the cytoplasm at around f_{cyto} = 1 MHz.[21] Finally, the current at f_{nuc} = 5 MHz passes through the nucleoplasm.[21] Therefore, $\Delta\mathbf{R}_{\mathrm{cyt}} = (\mathbf{R}_{f_{\mathrm{cyt}}} - a\mathbf{R}_{f_{\mathrm{ext}}})/\max(\mathbf{R}_{f_{\mathrm{ext}}})$

and $\Delta\mathbf{R}_{\mathrm{nus}} = (\mathbf{R}_{f_{\mathrm{nus}}} - a\mathbf{R}_{f_{\mathrm{cyt}}})/\max(\mathbf{R}_{f_{\mathrm{cyt}}})$ are applied to reconstruct the cytoplasm and nucleoplasm conductivities.

4.2 Reconstruction results

Fig. 4 shows the reconstruction results of three types of cells. Fig. 4(a) shows the cell structure, microscopy and reconstructed images of three types of cells. The cell structure images show that WT refers to the common type of MRC-5, HT is the MRC-5 transfected with green fluorescent protein (GFP)-fused histone in the nucleoplasm, and GFPT is the MRC-5 transfected with GFP in the cytoplasm, all of which leads to differences in intracellular conductivity distribution among the three cell types.[37] The microscopy images show the position and size of single cells. Fig. 4(b) shows the image processing using ImageJ software[38] to extract the position and size of a single cell, with HT as an example. In the image processing of the cytoplasm, two lines (Line 1 and Line 2) were first drawn across the approximate center of the cell on the EIT image. The gray value profiles along the two lines show peak values of $g_{\mathrm{max\text{-}Line1}} = 154.6$ and $g_{\mathrm{max\text{-}Line2}} = 149.2$, respectively. Based on comparisons between EIT images and microscopy images from multiple experiments, it was found that using $T = (g_{\max} - g_{\mathrm{base}})/2 + g_{\mathrm{base}}$ as the threshold T yielded a cytoplasmic diameter most consistent with that observed in microscopy, where g_{base} is the gray value of the baseline. The average of $T_{\mathrm{Line1}} = 90.1$ and $T_{\mathrm{Line2}} = 87.4$ calculated from the two lines was adopted as the final threshold $T_{\mathrm{cyt}} = 88.75$, and the region with gray values exceeding T_{cyt} was extracted as the cytoplasmic contour. Finally, the Feret diameter and the x- and y-coordinates of the cytoplasmic contour were measured. For image processing of the nucleoplasm, the same method as that used for the cytoplasm was applied, in which the region with gray values exceeding $T_{\mathrm{nuc}} = 117.4$ was extracted as the nucleoplasm contour. As a result, the diameters of the three types of cells were $d_{\mathrm{WT}} = 17.1$ μm, $d_{\mathrm{HT}} = 14.4$ μm and $d_{\mathrm{GFPT}} = 17.2$ μm. The EIT images show the position and size of the cytoplasm (calculated by $\Delta\mathbf{R}_{\mathrm{cyt}}$) and the nucleoplasm (calculated by $\Delta\mathbf{R}_{\mathrm{nus}}$), which are consistent with the microscopy images. The merged images show the relative positions and sizes of the cytoplasm and nucleoplasm, which are consistent with typical cellular structures.[39] Fig. 4(c) shows the comparison of cytoplasm coordinates and size between microscopy and EIT images of the three cell types. Since brightfield observation only captures the cells but not the nuclei, this section focuses solely on comparing the coordinates and sizes of the cytoplasm. The validation of the coordinates and sizes of the nuclei is addressed in the next section. The horizontal axis represents the x-coordinate, y-coordinate, and cytoplasm size d [μm], with the center of the micro-EIT sensor serving as the origin. The results show that the coordinates and sizes of the cytoplasm in EIT images of the three types of cells align with those observed in microscopy images. Fig. 4(d) shows the mean absolute errors (MAE [μm]) in diameter and the x and y coordinates between the EIT images and the microscopy images, which are calculated from multiple measurements of the three cell types. The MAE is calculated as follows:

$$\mathrm{MAE} = \frac{1}{N}\sum_{k=1}^{N}\left|u_{\mathrm{EIT}}^{(k)} - u_{\mathrm{microscopy}}^{(k)}\right| \tag{8}$$

where u represents either the x-coordinate, the y-coordinate, or the diameter, and MAE is calculated for each parameter individually. As a result, MAE for the x-coordinate, y-coordinate, or diameter is consistently around 1 μm, indicating a high level of accuracy. Fig. 4(e) shows the intracellular conductivity analysis of HT, where the green boundary represents the cell membrane, and the red boundary represents the nucleoplasm membrane from the EIT image. Using ImageJ software, the EIT images of the cytoplasm and nucleoplasm were each converted into 8-bit grayscale images, and the average grayscale values of the cytoplasm σ_{cyt} and nucleoplasm σ_{nuc} were then measured separately. The conductivity ratio $\sigma_{\mathrm{R}} = \sigma_{\mathrm{nuc}}/\sigma_{\mathrm{cyt}}$ was calculated to represent the intracellular conductivity distribution, serving as the parameter for cell identification. Fig. 4(f) shows σ_{cyt}, σ_{nuc} and conductivity ratio σ_{R} of the three cell types, where the black circles represent data points of σ_{cyt} and σ_{nuc}, the red squares indicate the mean values of σ_{cyt} and σ_{nuc}, and the black triangles represent σ_{R}. The σ_{R} of WT, considered to be normal cells, was regarded as a reference to analyse the impact of protein expression on conductivity. Compared to WT, histone–GFP is expressed in the nucleoplasm of HT, which decreased σ_{nuc}, while σ_{cyt} remained largely unchanged. On the other hand, GFP is expressed in the cytoplasm of GFPT, which increased σ_{cyt}, while σ_{nuc} remained largely unchanged. Based on the above conductivity changes, σ_{R} of the three cell types are $\sigma_{\mathrm{R\text{-}WT}} > \sigma_{\mathrm{R\text{-}GFPT}} > \sigma_{\mathrm{R\text{-}HT}}$, which serves as the parameter for cell identification.

4.3 Verification of nucleoplasm position and size

Fluorescence observation was applied to observe the position and size of the cell nucleoplasm to validate the EIT images. A fluorescent dye, DAPI (Cat. #5748, Tocris Bioscience, part of Bio-Techne, UK), with an excitation wavelength of 350 nm and an emission wavelength of 470 nm, was applied to stain the nucleoplasm of HT cells. A filter (49000-ET-DAPI, Chroma Technology, USA) with an excitation wavelength of 350 nm (bandwidth 50 nm) and an emission wavelength of 460 nm (bandwidth 50 nm) was used to excite and observe DAPI. A cell culture medium solution containing 0.5 μM DAPI was used to culture HT cells in an incubator for 30 min to stain the nucleoplasm. Subsequently, EIT measurements were performed using the same procedure as in previous EIT experiments, and brightfield (exposure time: 61 ms) and fluorescence (exposure time: 3 s) images were simultaneously recorded by the microscope. Fig. 5(a) shows the brightfield, fluorescence and EIT images. The brightfield and

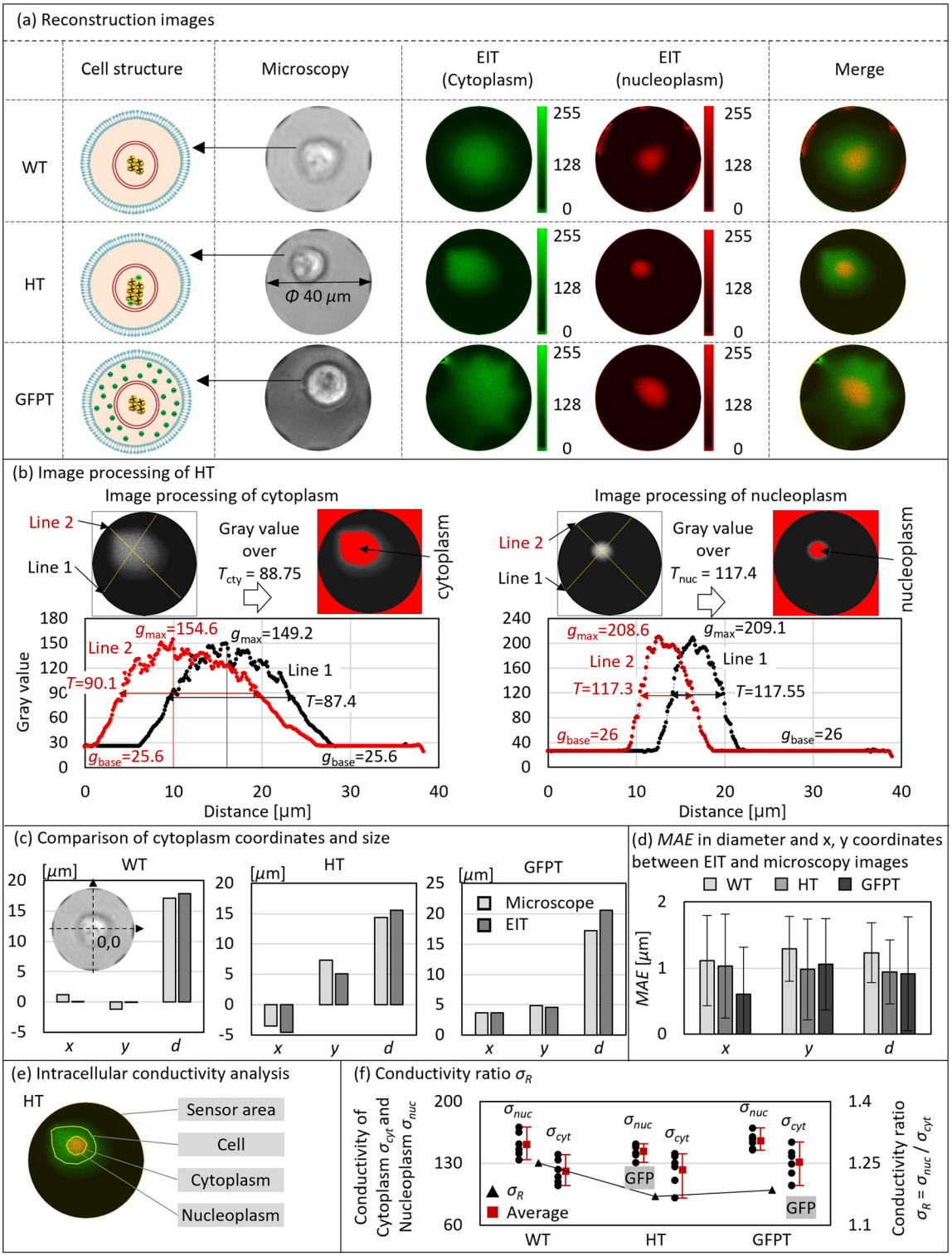

Fig. 4 Reconstruction results. (a) Structural schematic, microscopy images, and EIT reconstructed images of WT, HT and GFPT. (b) Image processing of reconstructed images to extract the position and size of the cytoplasm and nucleoplasm using gray value thresholding in ImageJ software, with HT as an example. (c) Comparison of cytoplasm coordinates and size between microscopy and reconstructed images. (d) Quantitative evaluation of reconstruction accuracy: MAE [μm] in diameter and *x*, *y* coordinates across multiple measurements. (e) Intracellular conductivity analysis to extract the mean conductivity of the cytoplasm and nucleoplasm. (f) σ_{cyto}, σ_{nuc} and conductivity ratio σ_R of WT, HT and GFPT.

fluorescence images show the position and size of the cell (cytoplasm) and nuclei (nucleoplasm) in the micro-EIT sensor. The Feret diameters of the cytoplasm and nucleoplasm are 18.8 μm and 11.8 μm, respectively, which

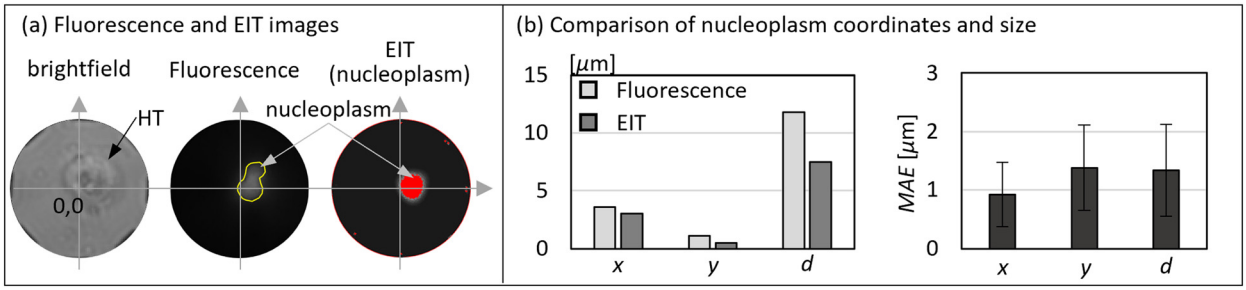

Fig. 5 Verification of nucleoplasm position and size. (a) Brightfield, fluorescence and EIT images. (b) Comparison of nucleoplasm *x*- and *y*-coordinates and size of fluorescence and EIT images (on the left) and MAE [μm] (on the right).

are in line with the general relationship between the size of the nucleoplasm and the cell in human cells.[40] The EIT image shows the position and size of the nucleoplasm, which aligns with the fluorescence image. Fig. 5(b) shows the comparison of nucleoplasm coordinates and size of fluorescence and EIT images, where the center of the sensor is the coordinate origin. The graph shown on the left, which is derived from the analysis of Fig. 5(a), demonstrates that the *x*-coordinate, *y*-coordinate and diameter of the nucleoplasm in both the fluorescence and the EIT images are closely aligned, which effectively validates the results of EIT. The graph on the right illustrates the MAE [μm] of the *x*-coordinate, *y*-coordinate and diameter across multiple measurements of the three cell types, with MAE calculated

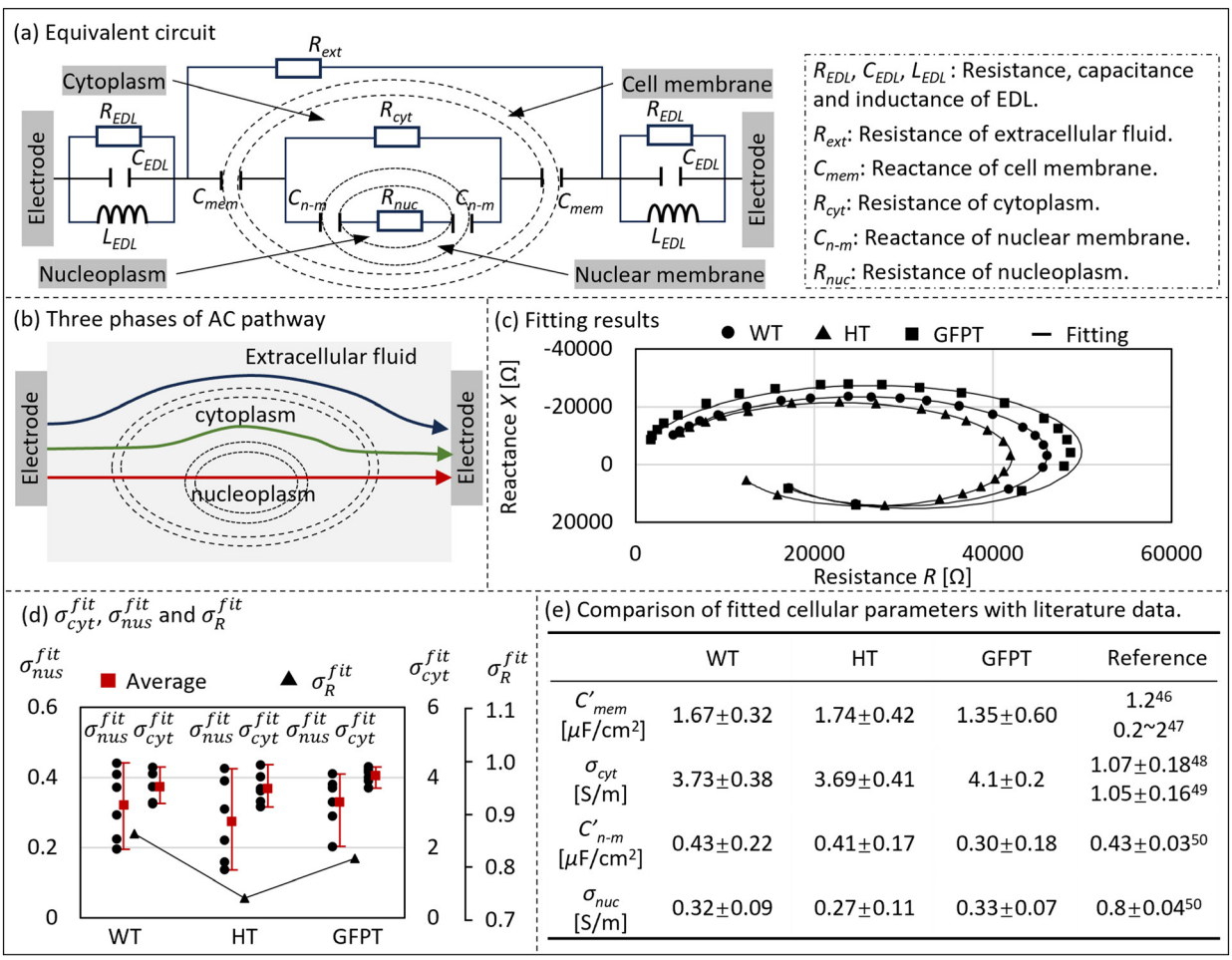

(e) Comparison of fitted cellular parameters with literature data.

	WT	HT	GFPT	Reference
C'_{mem} [μF/cm²]	1.67±0.32	1.74±0.42	1.35±0.60	1.2[46] 0.2~2[47]
σ_{cyt} [S/m]	3.73±0.38	3.69±0.41	4.1±0.2	1.07±0.18[48] 1.05±0.16[49]
$C'_{n\text{-}m}$ [μF/cm²]	0.43±0.22	0.41±0.17	0.30±0.18	0.43±0.03[50]
σ_{nuc} [S/m]	0.32±0.09	0.27±0.11	0.33±0.07	0.8±0.04[50]

Fig. 6 Electrical properties of a single cell. (a) Equivalent circuit which includes the components of the electric double layer (EDL) on the electrode surface, extracellular fluid, cell membrane, cytoplasm, nuclear membrane, and nucleoplasm. (b) Three phases of AC pathway. (c) Fitting results of WT, HT and GFPT. (d) Calculated conductivity of cytoplasm σ_{cyt}^{fit} and nucleoplasm σ_{nus}^{fit}, and conductivity ratio σ_R^{fit} based on fitted R_{cyt} and R_{nuc}. (e) Comparison of fitted cellular parameters of cytoplasm conductivity, nucleoplasm conductivity, cell membrane capacitance and nuclear membrane capacitance with literature data.

using eqn (8). The results show that MAE consistently remains around 1 μm, indicating a high level of accuracy.

4.4 Electrical properties of a single cell

An equivalent circuit including the elements extracellular fluid, cell membrane, cytoplasm, nuclear membrane and nucleoplasm was constructed to analyse the electrical properties of a single cell. Fig. 6(a) shows the equivalent circuit, which includes the resistance R_{EDL}, reactance C_{EDL} and inductance L_{EDL} of the electric double layer (EDL) on the electrode surface, resistance R_{ext} of the extracellular fluid, reactance C_{mem} of the cell membrane, resistance R_{cyt} of the cytoplasm, reactance $C_{n\text{-}m}$ of the nuclear membrane, and resistance R_{nuc} of the nucleoplasm. The parallel combination of resistance and capacitance is typically applied to represent the properties of the EDL at the electrode surface,[41] which represents the resistive behaviour arising from the finite conductivity of the electrolyte in the compact layer and the capacitive behaviour resulting from the charge separation across the diffuse layer.[42] Based on the measurement results of the PBS–sucrose solution shown in Fig. 3(a), an inductive component appears to be present in our system, which is potentially caused by electrode geometry, magnetic field interactions and electrochemical reaction kinetics.[43] Consequently, in addition to the parallel resistance–capacitance (RC) circuit typically used to model the electrical double layer, a parallel inductance element has been incorporated to more accurately represent the interfacial behaviour of our system. Fig. 6(b) shows the three phases of the alternating current (AC) pathway in blue, green and red, based on the capacitive properties of the cell membrane and nuclear membrane,[19] which provide the basis for the parallel relationship of the extracellular fluid, cytoplasm, and nucleoplasm elements shown in Fig. 6(a). At low frequency, AC (blue) is unable to penetrate the cells and primarily flows through the extracellular fluid, which is attributed to the high impedance presented by the insulating lipid bilayers of the cell membranes, effectively blocking AC flow into the intracellular space.[44] At intermediate frequency, AC (green) traverses the cell membrane and cytoplasm but still encounter a significant barrier at the nuclear membrane.[45] At high frequency (red), AC penetrates both the cell membrane and the nuclear membrane, allowing it to flow through the nucleoplasm. Fig. 6(c) shows the fitting results of WT, HT and GFPT, where the dot is the experimental result, and the line is the fitting result. To minimize the influence of EDL and extracellular fluid on the impedance response, a frequency-based modelling strategy was adopted. Parameters related to EDL and extracellular fluid components were first extracted from low-frequency data using a simplified equivalent circuit model without cellular elements. These parameters were subsequently fixed and incorporated into a complete equivalent circuit for fitting the cellular components. Although the introduction of a cell may slightly alter the properties of the surrounding EDL and extracellular fluid due to the exchange of materials between the intracellular and extracellular environments,[27] this stepwise modelling approach effectively reduces their influence. The fitting results demonstrate an exceptional agreement between the experimental impedance data and the proposed equivalent circuit. Fig. 6(d) shows the calculated conductivity of the cytoplasm σ_{cyt}^{fit} and nucleoplasm σ_{nus}^{fit}, and the conductivity ratio σ_{R}^{fit} of the three cell types, where the black circles represent data points of σ_{cyt}^{fit} and σ_{nus}^{fit}, the red squares indicate the mean values of σ_{cyt}^{fit} and σ_{nus}^{fit}, and the black triangles represent σ_{R}^{fit}. The σ^{fit} was calculated by $\sigma = d/RA$, where d is the diameter, R is the fitted resistance and $A = 4\pi(d/2)^2$ is the surface area of the cytoplasm or nucleoplasm. The average σ_{cyt}^{fit} and σ_{nus}^{fit} indicated that $\sigma_{cyt\text{-}WT}^{fit} \approx \sigma_{cyt\text{-}HT}^{fit} < \sigma_{cyt\text{-}GFPT}^{fit}$ due to the transfection of GFP in the cytoplasm of GFPT and $\sigma_{nuc\text{-}WT}^{fit} \approx \sigma_{nuc\text{-}GFPT}^{fit} > \sigma_{nuc\text{-}HT}^{fit}$ due to the transfection of GFP-fused histone in the nucleoplasm of HT. $\sigma_{R}^{fit} = \sigma_{nus}^{fit}/\sigma_{cyt}^{fit}$ shows that $\sigma_{R\text{-}WT}^{fit} > \sigma_{R\text{-}GFPT}^{fit} > \sigma_{R\text{-}HT}^{fit}$, which indicates the same trend in cell conductivity as the EIT results shown in Fig. 4(d). Fig. 6(e) shows the comparison of fitted cellular parameters with literature data, where σ_{cyt} [S m^{-1}] and σ_{nus} [S m^{-1}] are the conductivities of the cytoplasm and nucleoplasm, and C'_{mem} [μF cm^{-2}] and $C'_{n\text{-}m}$ [μF cm^{-2}] are specific capacitances of the cell membrane and nuclear membrane. For C'_{mem}, the fitted results of three types of cells are 1.67 ± 0.32, 1.74 ± 0.42 and 1.35 ± 0.60 μF cm^{-2}, which are consistent with the typical specific capacitance of cell membranes, reported to be 1.2 μF cm^{-2} (ref. 46) and within the range of 0.2–2 μF cm^{-2}.[47] For σ_{cyt}, the fitted results of three types of cells are 3.73 ± 0.38, 3.69 ± 0.41 and 4.1 ± 0.2 S m^{-1}, which are slightly higher than the reference values of 1.07 ± 0.18 S m^{-1} (ref. 48) and 1.05 ± 0.16 S m^{-1}.[49] For $C'_{n\text{-}m}$, the fitted result of three types of cells are 0.43 ± 0.22, 0.41 ± 0.17 and 0.30 ± 0.18 μF cm^{-2}, which are close to the reference value of 0.43 ± 0.03.[50] For σ_{nus}, the fitted results of three types of cells are 0.32 ± 0.09, 0.27 ± 0.11 and 0.33 ± 0.07 S m^{-1}, which are slightly lower than the reference value of 0.8 ± 0.04 S m^{-1}.[50] Although the fitted cellular parameters are on the same order of magnitude as the reference values, certain discrepancies exist. These differences may arise due to inherent variations among individual cells, differences in experimental conditions, and changes in cell states, all of which influence cellular parameters. Therefore, the fitted cellular parameters obtained in this study are considered reasonable and acceptable.

4.5 Potential applications and future directions

This study presents a proof-of-concept demonstration of a micro-EIT imaging system capable of reconstructing intracellular conductivity distributions at the single-cell level. Suspended cells with simple morphology were used to validate the system's feasibility, and three representative model cell types, WT representing normal

cells, HT with abnormal nuclear protein expression, and GFPT with abnormal cytoplasmic protein expression, were analyzed. The reconstructed conductivity of the cytoplasm and nucleoplasm revealed clear differences corresponding to subcellular protein expression, demonstrating that intracellular electrical properties can serve as biophysical markers to distinguish between different cell types or subtypes. The ability to extract such parameters in a non-invasive and label-free manner opens new possibilities for single-cell classification based on electrical signatures. Future work will focus on upgrading the micro-EIT system to enable real-time monitoring of more complex cell types, such as adherent cells, as well as tracking subcellular dynamics, including nuclear changes. These advancements will significantly broaden the applicability of this method in biomedical research, including applications in cancer diagnosis, stem cell monitoring, and drug response evaluation.

Our current system uses suspended cells and lays the foundation for future integration with microfluidic techniques.[1] In the current study, suspended cells were used, but they were not in a completely floating state. Once introduced into the measurement chamber, cells gradually settled due to gravity and temporarily adhered to the glass substrate of the micro-EIT sensor. In the absence of significant external disturbance, the cells remained stably positioned throughout the impedance measurements. To further ensure accurate and reproducible positioning, a pneumatic microinjector was employed to gently manipulate and guide individual cells toward the center of the sensing area. In addition, while our approach currently focuses on high-resolution, label-free imaging at the single-cell level, it holds strong potential to complement high-throughput methods such as impedance cytometry[51] and dielectric spectroscopy.[52] These established techniques are well suited for population-level classification based on average or bulk electrical properties[53] but generally lack subcellular spatial resolution. In contrast, our micro-EIT technique provides detailed conductivity mapping of cytoplasmic and nucleoplasm regions, serving as a powerful complementary tool to these methods in the spatial resolution at the subcellular scale. In future work, we plan to integrate microfluidic modules into the micro-EIT system, which will allow automated cell handling and position control, thereby improving throughput and enabling the transition from single-cell analysis to scalable studies that connect cellular heterogeneity with population-level electrical profiling.

5 Conclusions

This study proposed an electrical impedance tomography (EIT)-based single-cell imaging for cell identification *via* intracellular conductivity distribution by developing a micro-EIT imaging system with a single-cell scale sensor and incorporating fdEIT with spectral analysis.

(a) The EIT-based intracellular conductivity imaging was achieved by the development of a micro-EIT sensor with a sensor size of 40 μm combined with the application of frequency-difference EIT.

(b) The conductivities of the cytoplasm σ_{cyt} and nucleoplasm σ_{nuc} of three cell types were reconstructed by the proposed EIT-based intracellular conductivity imaging, where $\sigma_{cyt\text{-}WT} \approx \sigma_{cyt\text{-}HT} < \sigma_{cyt\text{-}GFPT}$ due to the transfection of GFP in the cytoplasm of GFPT and $\sigma_{nuc\text{-}WT} \approx \sigma_{nuc\text{-}GFPT} > \sigma_{cyto\text{-}HT}$ due to the transfection of GFP-fused histone in the nucleoplasm of HT. The conductivity ratio $\sigma_R = \sigma_{nuc}/\sigma_{cyto}$ was calculated to represent the intracellular conductivity distribution, which indicated $\sigma_{R\text{-}WT} > \sigma_{R\text{-}GFPT} > \sigma_{R\text{-}HT}$.

(c) Brightfield and fluorescence microscopy observations were performed to validate the EIT results, which confirmed the position and size of the cytoplasm and nucleoplasm.

(d) An equivalent circuit including the elements extracellular fluid, cell membrane, cytoplasm, nuclear membrane and nucleoplasm was constructed to analyze the electrical properties of a single cell. The calculated conductivities of the cytoplasm σ_{cyt}^{fit} and nucleoplasm σ_{nus}^{fit} indicated the same trend as the EIT results. The conductivity ratio σ_R^{fit} showed $\sigma_{R\text{-}WT}^{fit} > \sigma_{R\text{-}GFPT}^{fit} > \sigma_{R\text{-}HT}^{fit}$, which also indicated the same trend in cell conductivity as the EIT results.

Author contributions

Songshi Li: conceptualization, experiments, data analysis, methodology, writing and funding acquisition. Daisuke Kawashima: methodology, funding acquisition and review. Zeyang Dai: simulation. Nobuyuki Aoki: hardware and review. Masahiro Takei: funding acquisition, review and supervision.

Conflicts of interest

There are no conflicts to declare.

Data availability

All the original data can be provided upon request to the first author.

Acknowledgements

The authors would like to express their sincere appreciation to Dr. Michio Kida of Chiba University for his technical support in sensor design and fabrication and to Mr. Kodai Tsurumoto and Mr. Yuichiro Ikeda of Chiba University for their assistance with the experiments. This work was supported by the Japan Society for the Promotion of Science (JSPS) through the Grants-in-Aid for Scientific Research-Young Researchers (No. JP23K17186 and JP25K21547), Grants-in-Aid for Scientific Research-Challenging Research (No. JP23K18571), and the Fund for the Promotion of Joint International Research (No. JP23KK0090). This work was also supported by JSPS Program for Forming Japan's Peak Research Universities (J-PEAKS), Grant Number JPJS00420230002.

References

1 C. Honrado, P. Bisegna, N. S. Swami and F. Caselli, *Lab Chip*, 2021, **21**, 22–54.
2 A. Savva, J. Saez, A. Withers, C. Barberio, V. Stoeger, S. Elias-Kirma, Z. Lu, C.-M. Moysidou, K. Kallitsis and C. Pitsalidis, *Mater. Horiz.*, 2023, **10**, 3589–3600.
3 S. Arman, R. D. Tilley and J. J. Gooding, *Analyst*, 2024, **149**, 269–289.
4 T. R. L. C. Paixão, L. F. Barbosa, M. T. Carrì, M. H. G. Medeiros and M. Bertotti, *Analyst*, 2008, **133**, 1605–1610.
5 H. Matsuoka and M. Saito, *Electrochemistry*, 2006, **74**, 12–18.
6 L. Nan, Z. Jiang and X. Wei, *Lab Chip*, 2014, **14**, 1060–1073.
7 M. Thein, F. Asphahani, A. Cheng, R. Buckmaster, M. Zhang and J. Xu, *Biosens. Bioelectron.*, 2010, **25**, 1963–1969.
8 S. C. Bürgel, C. Escobedo, N. Haandbæk and A. Hierlemann, *Sens. Actuators, B*, 2015, **210**, 82–90.
9 L. Chen, Z. Han, X. Fan, S. Zhang, J. Wang and X. Duan, *Biosens. Bioelectron.*, 2020, **165**, 112374.
10 J.-L. Hong, K.-C. Lan and L.-S. Jang, *Sens. Actuators, B*, 2012, **173**, 927–934.
11 K. N. Dahl, A. J. S. Ribeiro and J. Lammerding, *Circ. Res.*, 2008, **102**, 1307–1318.
12 D. Kawashima, T. Yuki, S. Li and M. Takei, *Biosens. Bioelectron.*, 2022, 114432.
13 M. F. Ihsan, D. Kawashima, S. Li, S. Ogasawara, T. Murata and M. Takei, *Lab Chip*, 2024, **24**(12), 3183–3190.
14 X. Yin, H. Wu, J. Jia and Y. Yang, *IEEE Sens. J.*, 2018, **18**, 5402–5412.
15 Z. Liu, P. Bagnaninchi and Y. Yang, *IEEE Trans. Med. Imaging*, 2021, **41**, 983–996.
16 S. Li, D. Kawashima, Z. Gao and M. Takei, *IEEE Open J. Instrum. Meas.*, 2022, **1**, 1–9.
17 S. M. Weiz, P. Jha, K. Lee, R. Herzer, O. G. Schmidt and M. Medina-Sánchez, *Adv. Mater. Technol.*, 2023, **8**, 2300724.
18 C. Chuang, M. Mineharu, M. Matsunaga, C.-W. Liu, B.-Y. Wu, G.-H. Kim, K. Watanabe, T. Taniguchi, C.-T. Liang and N. Aoki, *Carbon*, 2019, **154**, 238–243.
19 A. Saxena and A. K. Dubey, *J. Phys. D: Appl. Phys.*, 2018, **52**, 015401.
20 E. O. Adekanmbi and S. K. Srivastava, *Lab Chip*, 2016, **16**, 2148–2167.
21 T. Tang, X. Liu, Y. Yuan, R. Kiya, Y. Shen, T. Zhang, K. Suzuki, Y. Tanaka, M. Li and Y. Hosokawa, *Lab Chip*, 2022, **22**, 550–559.
22 C. May, *Passive Circuit Analysis with LTspice*, Springer Nature Switzerland AG, Cham, 2020.
23 J. Yao, M. Sugawara, H. Obara, T. Mizutani and M. Takei, *IEEE Trans. Biomed. Circuits Syst.*, 2017, **11**, 1450–1458.
24 T. Mizutani, K. Takeda, H. Haga, M. Todo and K. Kawabata, *Histochem. Cell Biol.*, 2014, **141**, 473–481.
25 S. Li, D. Kawashima, K. O. Okeyo, T. Murata and M. Takei, *Meas. Sci. Technol.*, 2022, **34**, 035701.
26 T. Fischer-Cripps, *Newnes interfacing companion: computers, transducers, instrumentation and signal processing*, Elsevier, 2002.
27 S. Li, D. Kawashima, M. Sugawara, H. Obara, K. O. Okeyo and M. Takei, *Biomed. Phys. Eng. Express*, 2022, **8**, 035024.
28 D. Kawashima, S. Li, H. Obara and M. Takei, *IEEE Trans. Biomed. Eng.*, 2020, **68**, 1015–1023.
29 J. Yao and M. Takei, *IEEE Sens. J.*, 2017, **17**, 8196–8205.
30 A. Adler, *EIDORS version 3.10., Proceedings of the 20th International Conference on Biomedical Applications of EIT*, London UK, 2019, p. 63.
31 M. Vauhkonen, D. Vadász, P. A. Karjalainen, E. Somersalo and J. P. Kaipio, *IEEE Trans. Med. Imaging*, 1998, **17**, 285–293.
32 C. Wu and M. Soleimani, *IEEE Access*, 2019, **7**, 21870–21878.
33 Y. Wang, *Wiley Interdiscip. Rev. Comput. Stat.*, 2012, **4**, 415–420.
34 M. C. Estévez, R. Galve, F. Sánchez-Baeza and M. P. Marco, *Anal. Chem.*, 2005, **77**, 5283–5293.
35 R. A. Huggins, *Ionics*, 2002, **8**, 300–313.
36 C. Svensen, in *Pharmacology and Physiology for Anesthesia*, ed. H. C. Hemmings and T. D. Egan, Elsevier, Philadelphia, 2nd edn, 2019, pp. 814–835, DOI: **10.1016/B978-0-323-48110-6.00042-9**.
37 J. Yao, M. Sugawara, H. Obara, T. Mizutani and M. Takei, *IEEE Trans. Biomed. Circuits Syst.*, 2017, **11**, 1450–1458.
38 G. Fang, H. Lu, A. Law, D. Gallego-Ortega, D. Jin and G. Lin, *Lab Chip*, 2019, **19**, 4093–4103.
39 K. N. Dahl, A. J. S. Ribeiro and J. Lammerding, *Circ. Res.*, 2008, **102**, 1307–1318.
40 F. Guilak, J. R. Tedrow and R. Burgkart, *Biochem. Biophys. Res. Commun.*, 2000, **269**, 781–786.
41 J. Yao, L. Wang, K. Liu, H. Wu, H. Wang, J. Huang and J. Li, *Electrophoresis*, 2020, **41**, 1425–1432.
42 J. Wu, *Chem. Rev.*, 2022, **122**, 10821–10859.
43 J. Bisquert and A. Guerrero, *J. Am. Chem. Soc.*, 2022, **144**, 5996–6009.
44 C. Skourou, A. Rohr, P. J. Hoopes and K. D. Paulsen, *Phys. Med. Biol.*, 2006, **52**, 347.
45 H. Liang, Y. Zhang, D. Chen, H. Tan, Y. Zheng, J. Wang and J. Chen, *Micromachines*, 2019, **10**, 740.
46 S. Afshar, E. Salimi, A. Fazelkhah, K. Braasch, N. Mishra, M. Butler, D. J. Thomson and G. E. Bridges, *Anal. Chim. Acta*, 2019, **1059**, 59–67.
47 E. Sabri, S. Lasquellec and C. Brosseau, *Appl. Phys. Lett.*, 2020, **117**, 043701.
48 K. Wang, Y. Zhao, D. Chen, B. Fan, Y. Lu, L. Chen, R. Long, J. Wang and J. Chen, *Sci. Data*, 2017, **4**, 1–8.
49 K. Wang, Y. Zhao, D. Chen, C. Huang, B. Fan, R. Long, C.-H. Hsieh, J. Wang, M.-H. Wu and J. Chen, *Int. J. Mol. Sci.*, 2017, **18**, 1158.
50 A. Irimajiri, Y. Doida, T. Hanai and A. Inouye, *J. Membr. Biol.*, 1978, **38**, 209–232.
51 J. Chen, J. Zhong, H. Lei and Y. Ai, *Lab Chip*, 2023, **23**, 5029–5038.
52 F. D. Tehrani, M. D. O'Toole and D. J. Collins, *Lab Chip*, 2025, **25**, 837–855.
53 C. Honrado, A. Salahi, S. J. Adair, J. H. Moore, T. W. Bauer and N. S. Swami, *Lab Chip*, 2022, **22**, 3708–3720.